Effect of the inclusion of small metallic components in a two-dimensional dielectric photonic crystal with large full band gap

Chien C. Chang,[1] J. Y. Chi,[2] R. L. Chern,[1] C. Chung Chang,[1] C. H. Lin,[2] and C. O. Chang[1]
[1]*Institute of Applied Mechanics, National Taiwan University, Taipei 106, Taiwan, Republic of China*
[2]*Opto-Electronics & Systems Laboratories, Industrial Technology Research Institute, Hsinchu 310, Taiwan, Republic of China*
(Received 9 October 2003; revised manuscript received 1 March 2004; published 24 August 2004)

In this study, we investigate the effect of metallic inclusion modeled as perfect conductor on a dielectric photonic crystal (silicon/air) with large full band gap. The dielectric crystal consists of a hexagonal array of circular dielectric columns, each connected to its nearest neighbors by slender rectangular rods. It is found that inclusion of small metallic components inside the circular dielectrics sharply "turns off" the full band gap of the dielectric photonic crystal. By increasing the radius of metallic inclusion above a threshold value, the full band gap (of the metallodielectric photonic crystal) makes its appearance again and continues to grow in size. On the other hand, metallic inclusion in the air region shows an opposite trend that the full band gap is not turned off, and its size diminishes gradually to zero with increasing the radius of inclusion. These peculiar behaviors can be explained on a unified basis by examining different types of boundary conditions for TM and TE modes, and employing variational arguments based on Rayleigh's quotients. Moreover, the free-electron model for metallic components is also considered for TM modes. At large plasma frequencies, these modes show very close band structures to those described above for the case of perfect conductors.

DOI: 10.1103/PhysRevB.70.075108 PACS number(s): 78.20.Bh, 42.70.Qs, 02.70.Bf

I. INTRODUCTION

Photonic crystals are also known as photonic band-gap materials. The most attractive/distinguished feature of photonic crystals is their full band-gap structures.[1,2] Large full band gaps allow strong photon localization with the gap,[3,4] and a detailed manipulation of photonic defect states.[5,6] Intensive studies have been mainly concerned with dielectric materials. They have important applications such as microcavities,[7] optical waveguides,[8] defect mode lasers,[9] optical fibers[10] and feedback mirror in laser diodes.[11] Recently, photonic crystals comprising metal or metallodielectric materials have become increasingly important.

Photonic crystals with metallic components can possess much larger band gaps.[12–15] They may also act like nearly perfect reflectors.[16,17] New applications include high-impedance surfaces[18] and resonator gyrotron.[19] In addition, new electromagnetic phenomena are explored in metallic crystals such as a new forbidden band,[20] band gaps in the visible range,[21] strong capacitive coupling,[22] extraordinary optical transmission,[23] extremely low frequency plasmons,[24] surface enhanced Raman scattering[25] and a perfect lens.[26] Previous studies have shown that by including metallic components in the dielectric region the band gap can be significantly opened up or enlarged in three dimensions.[13,27] However, there are also disadvantages of using metals as they are usually quite lossy at optical frequencies.[20]

In the literature, there are three ways to model the metal property. The first one is to assume metals to be perfect conductors. The second one is to model metals as dispersive materials with the simple free-electron form of dielectric function. The third one is to model metals as dissipative materials with the Drude type of dielectric function. Therefore, metallodielectric photonic crystals could be modeled as combined structures of dielectric materials with one of the three types of metallic materials. In the present study, metallic components in photonic crystals are modeled as the perfect conductors. Moreover, we also consider dispersive metallic components with free-electron model for TM modes (*E* polarization). Compared to the dielectric counterpart, computation of photonic band structures for metallic or metallodielectric photonic crystals is more difficult. Below the plasma frequency, metals are able to reflect most of the electromagnetic radiations, and very little fields could sustain inside. Therefore, the electromagnetic field is compressed in the dielectric region, and may vary drastically in the case of large portion of metallic inclusion. This becomes even more severe for TE modes (*H* polarization), which intrinsically possess more irregular patterns. The computed eigenfunctions are more difficult to converge, especially at very long wavelengths.[28] In order to resolve the more complex structures of eigenfunctions, higher resolution and more efficient methods are necessary.

There are several approaches to the band structure computation of metallic and metallodielectric photonic crystals. The most widely used method for this purpose is plane wave expansion.[16,29–31] Other various techniques include the transfer matrix method,[32] the finite-difference time-domain method,[13,33–35] finite difference method,[17,28] generalized Rayleigh identity method,[36] the multiple multipole method[37] and the so-called order-*N* method.[38] In our previous paper, a highly fast and accurate inverse method with multigrid acceleration is developed to be applicable to photonic crystals comprising dielectric materials of arbitrary shape.[39] The developed algorithm is capable of resolving multieigenvalue band structures, and is applicable to photonic crystals with interfaces of strong contrast. In this study, we extend this method to be applicable to metallodielectric photonic crystals which contain both dielectric and perfectly conducting materials. The field inside the perfect conductor may be taken to be identically zero. Therefore, internal boundary conditions must be imposed on the conducting surfaces. The

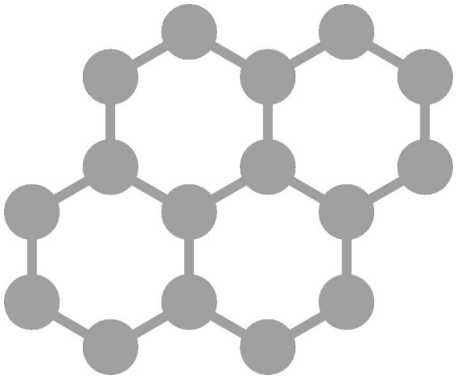

FIG. 1. Dielectric photonic crystal (silicon-air) consisting of a hexagonal array of circular cylinders, each connected to its nearest neighbors by slender rectangular rods.

eigensystem of the band structure remains a standard eigenvalue problem, as is the case of dielectric photonic crystals. Furthermore, the eigensystem preserves the Hermitian property and has real eigenfrequencies.

In the present study we are focused on the effect of metallic inclusion on band structures of dielectric photonic crystals. We start by considering a dielectric crystal (with lattice constant a) as the base structure, as shown in Fig. 1. The crystal consists of a hexagonal array of circular dielectric columns of radius r, each connected to its nearest neighbors by slender rectangular rods of width d.[39] The reason of choosing this geometry is as follows: previous studies indicate that band gaps for E polarization are favored in a lattice of isolated high-ε region, and band gaps for H polarization are favored in a connected lattice.[3] A compromise must therefore be reached between the sizes of the dielectric columns and the connecting rods in order to obtain an optimal full band gap. In fact, Fig. 2 shows that the optimal (and maximum) full band gap is attained when the band gaps for TM and TE modes have the simultaneous band gap, or the same band edges.[40]

Next, we consider circular columns of perfectly conducting material embedded inside the dielectric columns [Fig. 3(a)], or in the air region [Fig. 3(b)], to study the effect of metallic inclusion. The findings are several. The inclusion of metallic components in the dielectric region sharply "turns off" the full band gap of the dielectric photonic crystal, no matter how small is the size of the inclusion. The small size of metallic inclusion is advantageous for higher operating frequencies as the lossy effect will also be small. The band structure remains in the "off" state until the radius of inclusion reaches a threshold value. By increasing the radius of the metallic inclusion above the threshold value, the full band gap (of the metallodielectric photonic crystal) makes its appearance again. After that, the size of the full band gap increases monotonically with further increasing the radius of metallic inclusion. The latter result is consistent with early observations by other authors.[15,28] On the other hand, the inclusion of perfectly conducting materials in the air region does not "turn off" the full band gap of the dielectric photonic crystal. In this case the size of the full band gap decreases monotonically as the radius of inclusion is increased. All these peculiar behaviors can be explained on a unified basis by examining different types of boundary conditions imposed on TM and TE modes on the metal surfaces and employing variational arguments based on Rayleigh's quotients. Finally, interesting comparisons for the TM modes are made with the free-electron model for the metallic components at different plasma frequencies in the mode shapes and band structures.

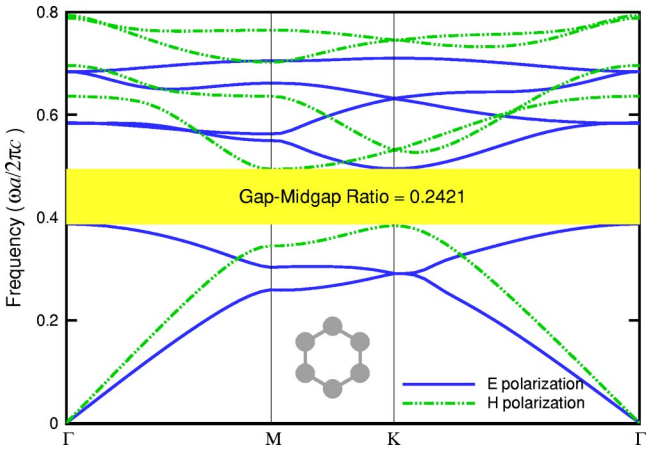

FIG. 2. (Color online) Band structure computed with a 256 $\times$256 grid for the dielectric photonic crystal in Fig. 1 with r/a =0.155 and d/a=0.035 for $\varepsilon/\varepsilon_0$=13.

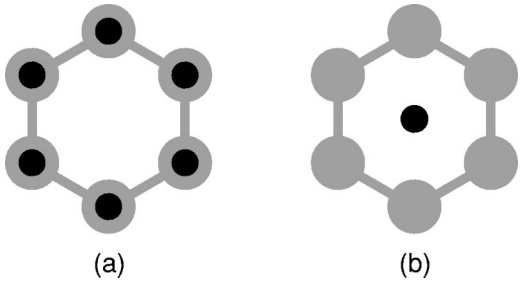

FIG. 3. Metallodielectric photonic crystal with metallic circular columns embedded (a) inside the dielectric columns (b) in the air region.

II. BASIC EQUATIONS AND NUMERICAL METHODS

For linear isotropic and frequency-independent dielectric materials with permeability close to one, the time-harmonic modes in two dimensions for E polarization (TM) can be written as

$$-\left(\frac{\partial^2}{\partial x^2}+\frac{\partial^2}{\partial y^2}\right)E=\varepsilon\left(\frac{\omega}{c}\right)^2E, \tag{1}$$

and H polarization (TE) as

$$-\left[\frac{\partial}{\partial x}\left(\frac{1}{\varepsilon}\frac{\partial}{\partial x}\right)+\frac{\partial}{\partial y}\left(\frac{1}{\varepsilon}\frac{\partial}{\partial y}\right)\right]H=\left(\frac{\omega}{c}\right)^2H, \tag{2}$$

where $E=E_z$ and $H=H_z$ are the electric and magnetic field intensities, respectively, and $\varepsilon=\varepsilon(\mathbf{r})$ is the dielectric function. To discretize Eqs. (1) and (2), a second order central

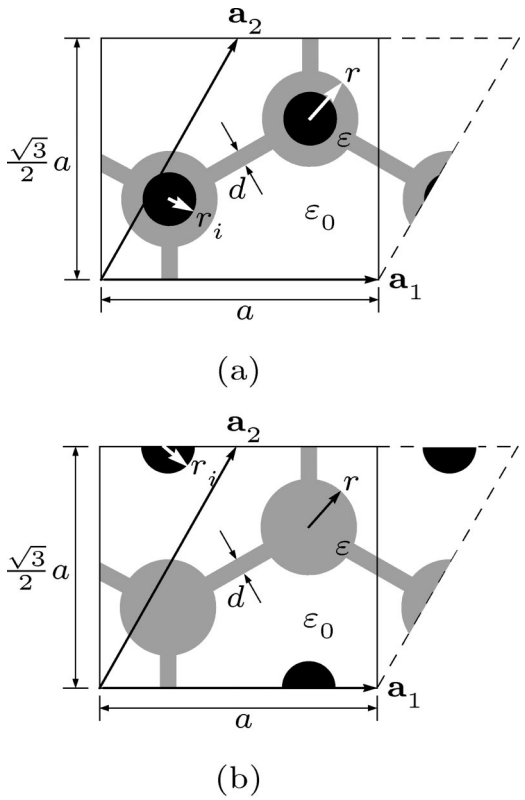

FIG. 4. Domain of computation for the metallodielectric photonic crystal with metallic circular columns embedded (a) inside the dielectric columns (b) in the air region.

finite difference scheme is used. Inside the perfect conductor, the electric field E vanishes, and the magnetic field H may be taken to be zero. The boundary condition on the perfectly conducting surface for E and H polarizations are, respectively,

$$E = 0 \quad \text{and} \quad \frac{\partial H}{\partial n} = 0, \tag{3}$$

where $\partial/\partial n$ is the normal derivative at a point on the surface.[41] In the present study, we also consider the dispersive free-electron model for the metallic components,

$$\varepsilon(\omega) = 1 - \frac{\omega_p^2}{\omega^2}, \tag{4}$$

where ω_p is the plasma frequency. In particular, we compute the band structures for E polarization. The eigenvalue problem outside the metallic region is described by Eq. (1) while inside the metallic region it can be recast to the following form:

$$\left[-\left(\frac{\partial^2}{\partial x^2} + \frac{\partial^2}{\partial y^2} \right) + \left(\frac{\omega_p}{c} \right)^2 \right] E = \left(\frac{\omega}{c} \right)^2 E. \tag{5}$$

For periodic structures, the domain of computation can be chosen as one unit cell along with suitable boundary conditions. For convenience of finite difference formulation, the domain of computation is chosen as a rectangle with the same area of the primitive cell of the hexagonal lattice as shown in Fig. 4. Bloch's theorem is applied at the domain boundary:

$$E_{\mathbf{k}}(\mathbf{r} + \mathbf{a}_i) = e^{i\mathbf{k}\cdot\mathbf{a}_i} E_{\mathbf{k}}(\mathbf{r}), \tag{6}$$

$$H_{\mathbf{k}}(\mathbf{r} + \mathbf{a}_i) = e^{i\mathbf{k}\cdot\mathbf{a}_i} H_{\mathbf{k}}(\mathbf{r}), \tag{7}$$

where $E_{\mathbf{k}}$ and $H_{\mathbf{k}}$ are the Bloch functions for the electric and magnetic fields, respectively, associated with the wave vector $\mathbf{k}$ in the first Brillouin zone, and $\mathbf{a}_i$ $(i=1,2)$ is the lattice translation vector. For the hexagonal lattice, $\mathbf{a}_1 = a(1,0)$ and $\mathbf{a}_2 = a(1/2, \sqrt{3}/2)$. Since $\mathbf{a}_2$ makes 60 degrees with the x-axis, the application of Bloch's condition in the y-direction should be additionally accompanied by one half cell in the x-direction.

From the practical point of view, the first few branches of eigenvalues are of primary interest. As a first step, it is natural for us to propose the method of inverse iteration[42,43] to compute the eigenvalues as well as eigenvectors from the smallest one. Let $\mathbf{A}$ be the discretization matrix of the differential operators in Eq. (1) or (2) or (5). The method of inverse iteration is based on the following equations:

$$(\mathbf{A} - \mu\mathbf{I})\mathbf{x} = \mathbf{v}. \tag{8}$$

The basic idea is to choose μ close to the smallest eigenvalue one wishes to compute and do the following steps.

(1) Compute the first eigenpair: (a) Pick up a random vector as the initial $\mathbf{v}$. (b) Solve Eq. (8) for $\mathbf{x}$ and replace $\mathbf{v}$ by the normalized $\mathbf{x}$. (c) Repeat step (b) until $\|\mathbf{A}\mathbf{v} - \lambda\mathbf{v}\|_2 < \epsilon$, where ϵ is a small number. The eigenvalue is obtained by the Rayleigh quotient $\langle \mathbf{v}, \mathbf{A}\mathbf{v} \rangle$. The first eigenpair is denoted by $(\lambda_1, \mathbf{q}_1)$.

(2) Compute the second eigenpair: (a) Pick up a random vector as the initial $\mathbf{v}$. (b) Solve Eq. (8) for $\mathbf{x}$ and deflate the components of $\mathbf{x}$ in the direction of the first eigenvector $\mathbf{q}_1$ by

$$\mathbf{x} \leftarrow \mathbf{x} - \langle \mathbf{q}_1, \mathbf{x} \rangle \mathbf{q}_1. \tag{9}$$

Replace $\mathbf{v}$ by the normalized $\mathbf{x}$. (c) Repeat step (b) until $\|\mathbf{A}\mathbf{v} - \lambda\mathbf{v}\|_2 < \epsilon$, where ϵ is a small number. The eigenvalue is obtained by the Rayleigh quotient $\langle \mathbf{v}, \mathbf{A}\mathbf{v} \rangle$. The second eigenpair is denoted by $(\lambda_2, \mathbf{q}_2)$.

(3) Compute the nth eigenpair: (a) Pick up a random vector as the initial $\mathbf{v}$. (b) Solve Eq. (8) for $\mathbf{x}$ and deflate the components of $\mathbf{x}$ in the directions of the first $n-1$ eigenvectors $\mathbf{q}_1 \ldots \mathbf{q}_{n-1}$ by

$$\mathbf{x} \leftarrow \mathbf{x} - \sum_{k=1}^{n-1} \langle \mathbf{q}_k, \mathbf{x} \rangle \mathbf{q}_k. \tag{10}$$

Replace $\mathbf{v}$ by the normalized $\mathbf{x}$. (c) Repeat step (b) until $\|\mathbf{A}v - \lambda\mathbf{v}\|_2 < \epsilon$, where ϵ is a small number. The eigenvalue is obtained by the Rayleigh quotient $\langle \mathbf{v}, \mathbf{A}\mathbf{v} \rangle$. The nth eigenpair is denoted by $(\lambda_n, \mathbf{q}_n)$.

The algorithm of inverse iteration is designed as follows:

InverseEigen {
for $n=1$ to S
Initial guess $\mathbf{v}$
do
Solve $(\mathbf{A}-\mu\mathbf{I})\mathbf{x}=\mathbf{v}$ by **LUD** or **PCG**
Deflate $\mathbf{x}$ by $\mathbf{q}_1$ to $\mathbf{q}_{n-1}$
Set $\mathbf{v}=\mathbf{x}/\|\mathbf{x}\|$
Rayleigh Quotient $\lambda_n=\langle\mathbf{v},\mathbf{Av}\rangle$
until $\|(\mathbf{A}-\lambda_n\mathbf{I})\mathbf{v}\|_2<\epsilon$
Set $\mathbf{q}_n=\mathbf{v}$
end }

where $\lambda_1\leqslant\lambda_2\leqslant\cdots\leqslant\lambda_S$ is the sequence of smallest eigenvalues, and $\mathbf{q}_1\ldots\mathbf{q}_S$ are the corresponding eigenvectors. The inner product $\langle\cdot,\cdot\rangle$ is defined as

$$\langle\mathbf{x},\mathbf{y}\rangle=\sum_i w_i\bar{x}_i y_i, \quad w_i=\begin{cases}\varepsilon(\mathbf{r}_i), & \text{for } E \text{ polarization;}\\ 1, & \text{for } H \text{ polarization}\end{cases}$$

in view of the different orthogonal properties of the E field and the H field:

$$\frac{1}{V_{cell}}\int V_{cell}\varepsilon(\mathbf{r})E_m^*(\mathbf{r})E_n(\mathbf{r})d\mathbf{r}=\delta_{mn}, \tag{11}$$

$$\frac{1}{V_{cell}}\int V_{cell}H_m^*(\mathbf{r})H_n(\mathbf{r})d\mathbf{r}=\delta_{mn}, \tag{12}$$

where E_n and H_n are the nth eigenfunctions of the electric and magnetic fields, respectively. V_{cell} denotes the volume of the primitive cell and δ_{mn} is the Kronecker delta. **LUD** denotes the LU decomposition solver for matrix inversion, and **PCG** the preconditioned conjugate gradient solver.

In the previous study, we proposed an idea to accelerate the convergence of matrix inversion in the algorithm. The idea is to embed inverse iteration in the multigrid acceleration structure. The basic idea of the multigrid method[44,45] is to solve the matrix problem by approximating the solution on a fine grid, solving the residue on a coarse grid, and then improving the solution on the fine grid. Successively applying this idea on multilevel of grids causes a relaxation of errors on different resolution, and hence accelerates the convergence of inverse iteration.

Let there be L levels of grids. On each grid level m, the differential operator is discretized to form the matrix $\mathbf{A}^{(m)}$. The inverse method with multigrid acceleration is implemented by the following steps.

TABLE I. Computing times in CPU seconds for the first six eigenmodes at point K for the metallodielectric photonic crystal in Fig. 3(a) with different r_i/a.

N_{grid}	No metals	$r_i/a=0.01$	$r_i/a=0.02$	$r_i/a=0.05$
64×64	0.203	0.297	0.297	0.438
128×128	0.937	1.391	1.25	1.422
256×256	3.844	6.922	7.672	6.844
512×512	12.828	42.125	27.359	32.422
1024×1024	39.641	179.187	108.171	155.125

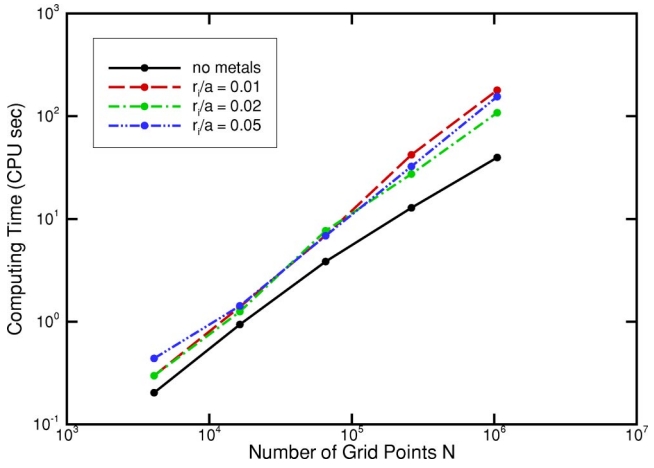

FIG. 5. (Color online) Computing times in CPU seconds for the first six eigenmodes at point K for the metallodielectric photonic crystal in Fig. 3(a) with different r_i/a.

(1) Given random vectors as the initial guesses, compute the first n eigenpairs $(\lambda_1^{(1)},\mathbf{q}_1^{(1)})\ldots(\lambda_n^{(1)},\mathbf{q}_n^{(1)})$ on the coarsest grid level by the inverse algorithm described previously.

(2) Interpolate $\mathbf{q}_1^{(1)}\ldots\mathbf{q}_n^{(1)}$ to the next finer grid level as the initial guesses. Replace **LUD** in the inverse algorithm by the multigrid V-cycle solver,[44,45] and compute the first n eigenpairs $(\lambda_1^{(2)},\mathbf{q}_1^{(2)})\ldots(\lambda_n^{(2)},\mathbf{q}_n^{(2)})$ on this grid level.

(3) Repeat step (2) until the eigenpairs on the finest grid level are obtained.

The algorithm of multilevel inverse iteration is designed as follows:

FMGInverse {
Call **InverseEigen** at $m=1$
for $m=2$ to L
for $n=1$ to S
Interpolate $\mathbf{q}_n^{(m-1)}$ to $\mathbf{v}^{(m)}$
do
Solve $(\mathbf{A}^{(m)}-\mu\mathbf{I})\mathbf{x}^{(m)}=\mathbf{v}^{(m)}$ by **MGV**
Deflate $\mathbf{x}^{(m)}$ by $\mathbf{q}_1^{(m)}$ to $\mathbf{q}_{n-1}^{(m)}$
Set $\mathbf{v}^{(m)}=\mathbf{x}^{(m)}/\|\mathbf{x}^{(m)}\|$
Rayleigh Quotient $\lambda_n^{(m)}=\langle\mathbf{v}^{(m)},\mathbf{A}^{(m)}\mathbf{v}^{(m)}\rangle$
until $\|(\mathbf{A}^{(m)}-\lambda_n^{(m)}\mathbf{I})\mathbf{v}^{(m)}\|_2<\epsilon$
Set $\mathbf{q}_n^{(m)}=\mathbf{v}^{(m)}$
end
end}

Notice that in the above algorithm, the Rayleigh quotient is

TABLE II. Convergence test for the full band gap against the grid size for the metallodielectric photonic crystal in Fig. 3(a) with $r_i/a=0.1$.

N_{grid}	128^2	256^2	512^2	1024^2
$a\omega_{up}/2\pi c$	0.5392	0.547	0.547	0.5457
$a\omega_{low}/2\pi c$	0.3639	0.3627	0.3538	0.3534
$a\omega_{mid}/2\pi c$	0.4516	0.4549	0.4504	0.4496
$a\Delta\omega/2\pi c$	0.1753	0.1843	0.1932	0.1923
$\Delta\omega/\omega_{mid}$	0.3882	0.4062	0.429	0.4278

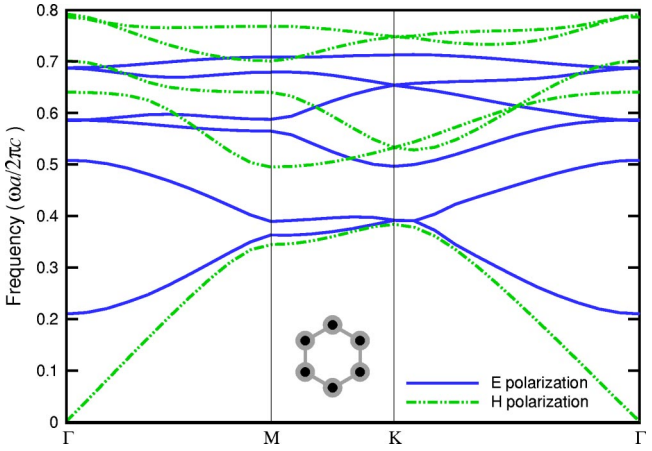

FIG. 6. (Color online) Band structure computed with a 256 $\times$256 grid for the metallodielectric photonic crystal in Fig. 3(a) with $r_i/a=0.01$.

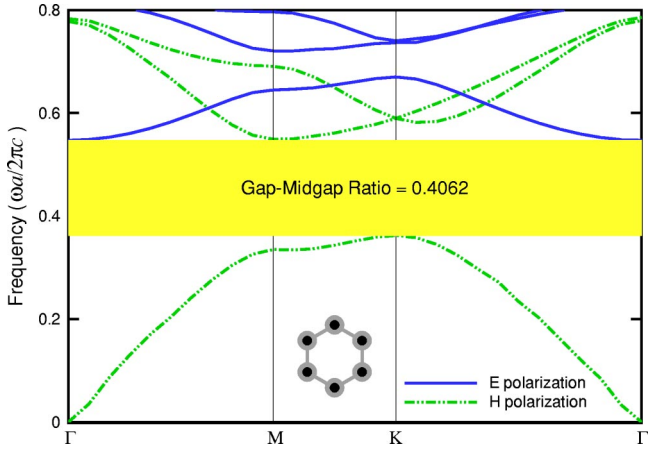

FIG. 8. (Color online) Band structure computed with a 256 $\times$256 grid for the metallodielectric photonic crystal in Fig. 3(a) with $r_i/a=0.1$.

updated after each multigrid V-cycle solver which may provide only an approximate solution to the inverse equation. As a result, the Rayleigh quotient updates more frequently and converges faster to the eigenvalue. The whole idea of proposing an inverse method with multigrid acceleration for computing photonic band structures has now become clear. First of all, the boundary condition (3) is used to take care of perfectly conducting inclusions. Second, the deflation in the algorithm of inverse iteration enables singling out the eigenvalues one by one from the smallest even when they may be degenerate. Third, interlacing the inverse iteration and multigrid acceleration makes the whole method an amazingly fast algorithm for computing photonic band structures, as demonstrated below.

III. RESULTS AND DISCUSSION

In this study, we consider the dielectric crystal in Fig. 1 as the base structure with fixed $r/a=0.155$ and $d/a=0.035$ for $\varepsilon/\varepsilon_0=13$. As an example of the test, we compute the first six frequency bands at point K for the metallodielectric photonic crystal by embedding circular columns of perfect conductors in the base structure. Table I lists the computing times in central processing unit (CPU) seconds for different radii of metallic inclusion. The computations are performed on a Pentium 4-2.8 GHz PC. Figure 5 shows a plot of these computing times, which demonstrates that the present method is of good order $N=N_{grid}$.

The convergence of the computed results against the grid size is illustrated by computations performed on four different grids: 128^2, 256^2, 512^2, and 1024^2. Table II lists the results of the band edges (ω_{up}, ω_{low}), midgap frequency (ω_{mid}), band width ($\Delta\omega$) and gap-midgap ratio ($\Delta\omega/\omega_{mid}$) for the metallodielectric photonic crystal in Fig. 3(a) with $r_i/a=0.1$ for the grid $N_{grid}\geqslant 128\times 128$. It can be seen that the numerical results for different grids fluctuate mildly but are in generally good agreement with each other. In the present study, the grid size $N_{grid}=256\times 256$ will be used in most computations.

Let us now start to study the effect of metallic inclusion shown in Fig. 3(a) by increasing the radius of inclusion r_i/a.

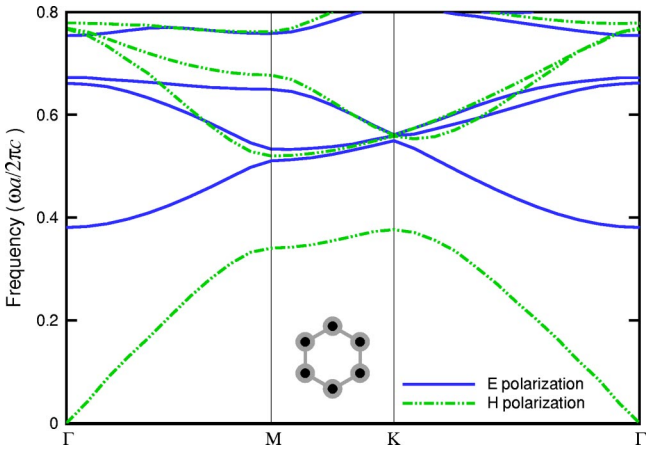

FIG. 7. (Color online) Band structure computed with a 256 $\times$256 grid for the metallodielectric photonic crystal in Fig. 3(a) with $r_i/a=0.06$.

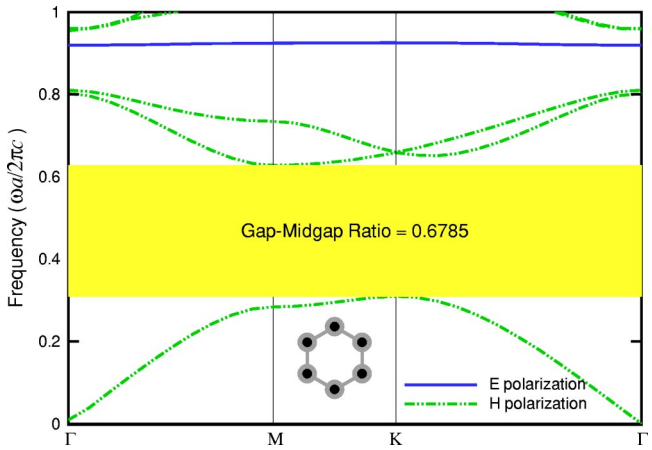

FIG. 9. (Color online) Band structure computed with a 256 $\times$256 grid for the metallodielectric photonic crystal in Fig. 3(a) with $r_i/a=0.2$.

Figures 6–9 present the band structures computed with a 256×256 grid, respectively, for $r_i/a=0.01$, 0.06, 0.1 and 0.2. At the small $r_i/a=0.01$, there is no longer a full band gap, and for which we say that the metallic inclusion sharply "turns off" the full band gap of the dielectric photonic crystal. In a comparison of Fig. 6 with Fig. 2, we observe that the first two branches of TM modes suddenly shift upward, trespassing into the region of the original full band gap, blocking it completely. The TE modes are relatively inactive to metal inclusion, and the band structure almost remains unchanged. The trend of the upward shift of TM modes continues. As r_i/a is increased to about 0.06 (Fig. 7), the full band gap remains in the "off" state. However, the lower edge of the first TM branch is about to move away from the upper edge of the first TE branch. Meanwhile, the band gap of the TE modes is widening in size. After this threshold value ($r_i/a=0.06$), the full band gap makes its appearance again, soon becoming widely open as the radius r_i/a is further increased. At $r_i/a=0.1$, the lower edge of the first TM branch approaches the upper edge of the widely opened band gap of the TE modes. At even larger r_i/a, the upward-shifted TM modes have moved completely out of the region of TE band gap, leaving the full band gap size to be solely determined by the TE modes. In the meantime, the first few branches of TM modes are flattening out with the group velocity almost identically zero (Fig. 9). These phenomena demonstrate that the metallodielectric photonic crystals behave more like metallic photonic crystals at large r_i/a. This can be reasonably expected because at $r_i/a=0.155$ the metal inclusions have already replaced in full the circular dielectric columns ($r/a=0.155$). As the metallic components become large enough, the eigenfrequencies of TM modes tend to be flattened out.[36] Eventually these TM modes become standing waves with no dispersion. In the limiting case when the conducting materials connect to each other, both TM and TE band structures are straight lines.[30] This is a typical behavior of the resonant modes of cavity.[46] They are standing waves confined and resonant in the dielectric region with eigenfrequencies independent of the wave vectors. The propagation of electromagnetic waves is shielded and neither electric field nor magnetic field could penetrate the conducting materials.

The behaviors observed may be explained by considering the different types of boundary conditions in (3) for TM and TE modes, and employing the variational argument based on the Rayleigh quotients:

$$Q_{TM}=\frac{\int_{V_{cell}}|\nabla E|^2 d\tau}{\int_{V_{cell}}\varepsilon|E|^2 d\tau}, \tag{13}$$

$$Q_{TE}=\frac{\int_{V_{cell}}\frac{1}{\varepsilon}|\nabla H|^2 d\tau}{\int_{V_{cell}}|H|^2 d\tau}, \tag{14}$$

respectively, for TM and TE modes, where we recall that V_{cell} denotes the volume of the primitive cell. The inclusion of metallic materials significantly modifies the band structure of TM modes by introducing a zeroth-order band gap,[28] which is analogous to the cutoff behavior of conventional waveguides. However, the origin of the cutoff behavior for the TM modes of the metallodielectric photonic crystal is very different from that of the conventional waveguide. In the conventional waveguide, the cutoff frequency originates from the sustenance of transverse oscillations,[46] while in the metallodielectric photonic crystals, the electric fields are identically zero inside and on the surface of the perfect conductors. In particular, consider the TM modes at the symmetric point Γ. If the zero-frequency solution (without a cutoff frequency) is allowed in the crystal, the electric field should be constant everywhere outside the perfect conductors. By the continuity of the electric field at the metal boundary ($E=0$), this constant must be zero, resulting in a trivial solution. Therefore, TM modes with zero frequency do not exist, making an appearance of the cutoff frequency. On the other hand, the cutoff behavior is not observed in TE modes for metallodielectric crystals. This is because constant solutions with zero frequency are allowed in the crystal without violating the boundary condition ($\partial H/\partial n=0$) for TE modes.

The variational analysis based on (13) and (14) argues that both TM and TE modes favor accommodation of their eigenfunctions in high-ε regions in order to minimize the Rayleigh's quotients. However, because of the different boundary conditions, the inclusion of metallic components repels the eigenfunctions of TM modes outward from the inclusion more effectively than those of TE modes. In the first place, we consider the dielectric photonic crystal in Fig. 1 and plot the first three eigenfunctions in magnitude at point Γ for TM modes in Fig. 10 and for TE modes in Fig. 11. Since there are no internal boundary conditions, both modes allow zero-frequency eigenfunctions. As expected, all the eigenfunctions except the zero-frequency ones are concentrated on and around the higher-ε circular regions, but the TM eigenfunctions are more spread out. For a strong contrast, we next consider the metallodielectric photonic crystal in Fig. 3(a) with $r_i/a=0.02$ and plot the first three eigenfunctions in magnitude at point Γ for TM modes in Fig. 12 and for TE modes in Fig. 13. For TM modes, the argument based on the boundary condition has excluded the possibility of constant eigenfunctions. All the three eigenfunctions rise sharply from 0 at the metal surface to peak values, causing large gradients in the eigenfunctions and thus contributing to the sudden upshift of the eigenvalues. On the other hand, the boundary condition for TE modes does allow constant eigenfunctions, and only requires at the metal surface a round shape of the eigenfunctions around the rim of the metal inclusion. This requirement does not change effectively the TE bands and the shapes of the corresponding eigenfunctions. There is one further comparison with the case of dielectric photonic crystals that for either TM or TE modes, the eigenfunctions of the metallodielectric photonic crystals tend to be even more concentrated on and near the annular high-ε regions for better minimization of the Rayleigh's quotients. This is no longer possible if the radius of metal inclusion r_i/a comes close to that of the dielectric circular columns $r/a=0.155$. The eigenfunction of the first TM mode rises more abruptly from 0, while the first TE mode can adjust itself to be an even smoother function.

Figure 14 shows the gap map computed with a 128×128 grid for the metallodielectric photonic crystal in Fig.

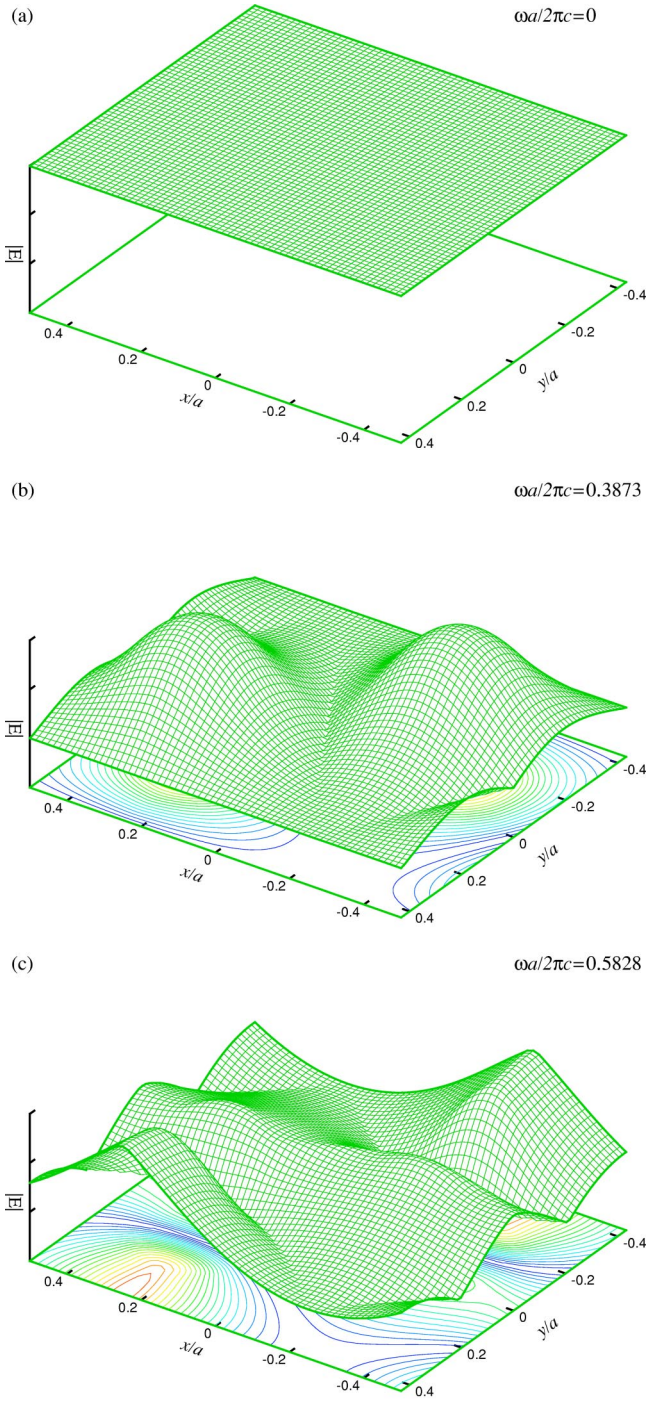

FIG. 10. (Color online) The first three TM eigenfunctions in magnitude at point Γ for the dielectric photonic crystal in Fig. 1.

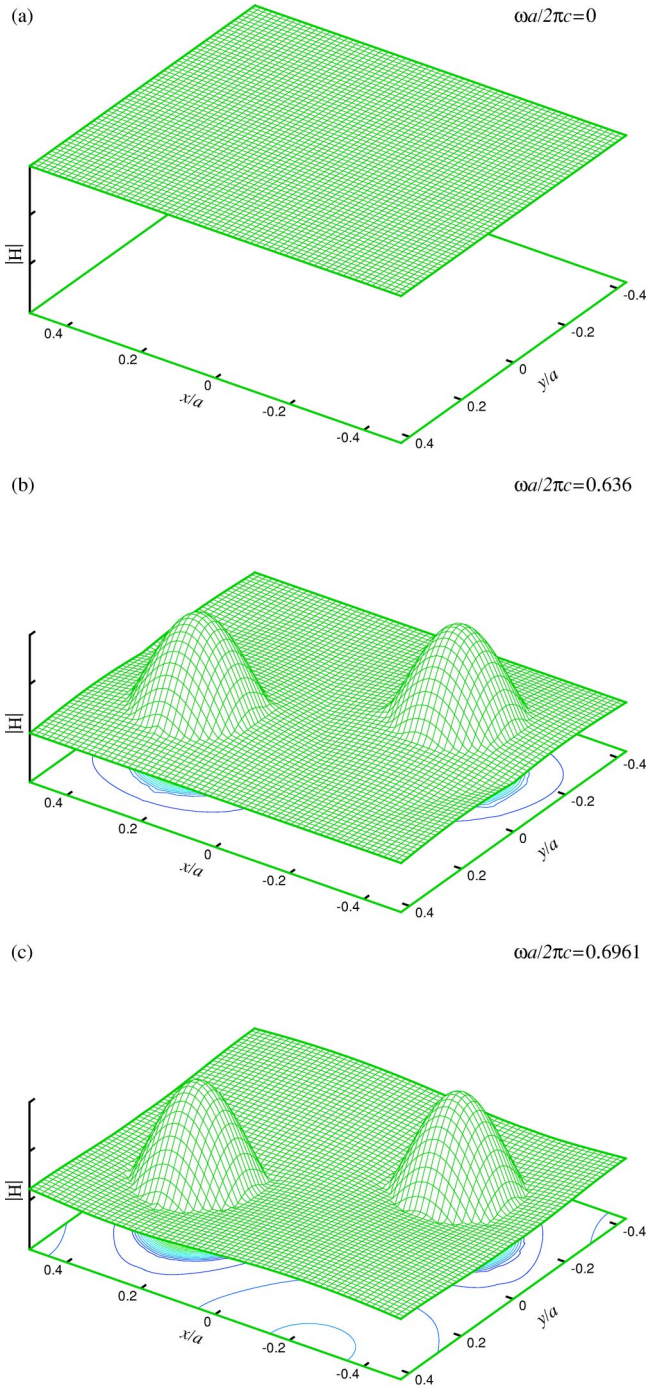

FIG. 11. (Color online) The first three TE eigenfunctions in magnitude at point Γ for the dielectric photonic crystal in Fig. 1.

3(a) by varying the radius r_i/a. As the shifted TM bands are trespassing into the original band gap region of the dielectric photonic crystals, the band structure remains in the "off" state. By increasing the size of the metallic inclusion above a threshold value, the full band gap (of the metallodielectric photonic crystals) opens again and its size continues to grow as the upward shifted TM bands are moving away from the upper band edge of the TE band gap. In this case, the threshold value of the metallic inclusion is about $r_i/a=0.06$, and the corresponding band structure at this inclusion is shown in Fig. 7. It is noticed that for large size of metallic inclusion, the full band gap is very large because the zeroth-order band gap for the TM mode covers the whole band gap for TE mode. This phenomenon was also identified in Ref. 28.

On the other hand, we consider metallic inclusions in the air region, as shown in Fig. 3(b). The full band gap decreases monotonically in size and finally diminishes to zero with increasing the radius r_i/a of metallic inclusion. Figure 15 shows the gap map computed with a 128×128 grid by varying the radius r_i/a. It is observed that the cutoff behavior for

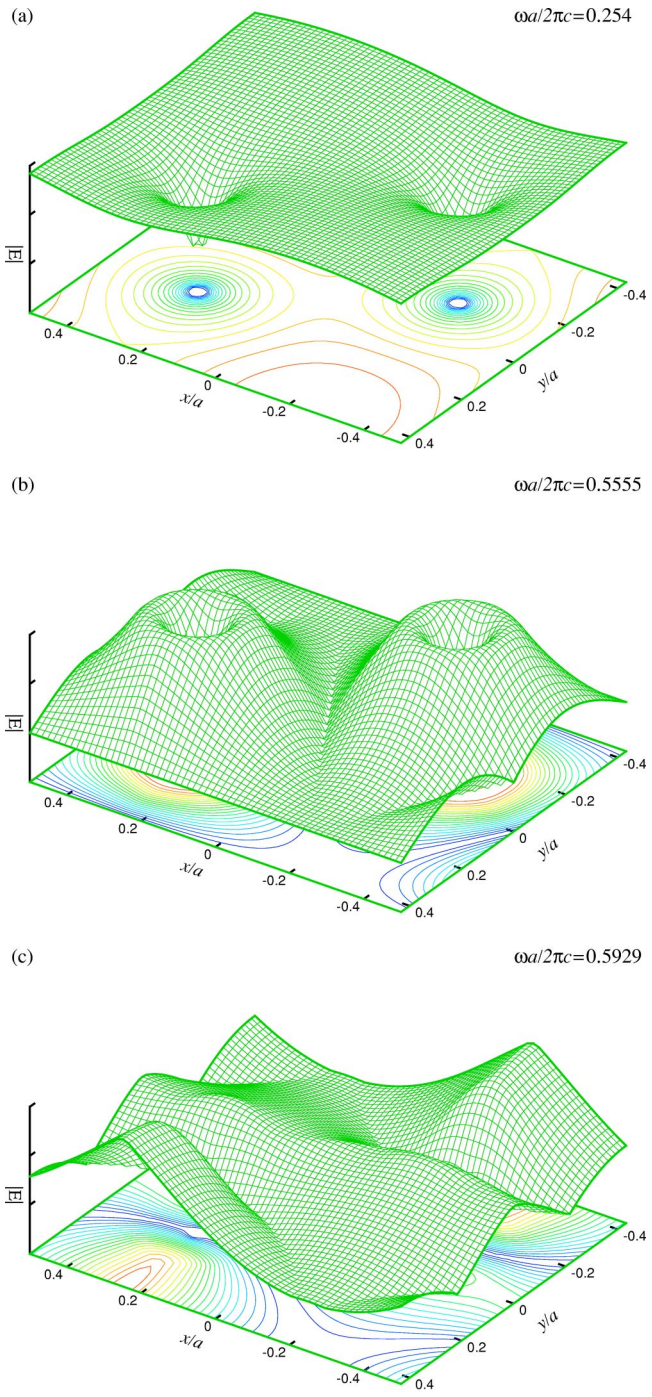

FIG. 12. (Color online) The first three TM eigenfunctions in magnitude at point Γ for the metallodielectric photonic crystal in Fig. 3(a) with $r_i/a=0.02$.

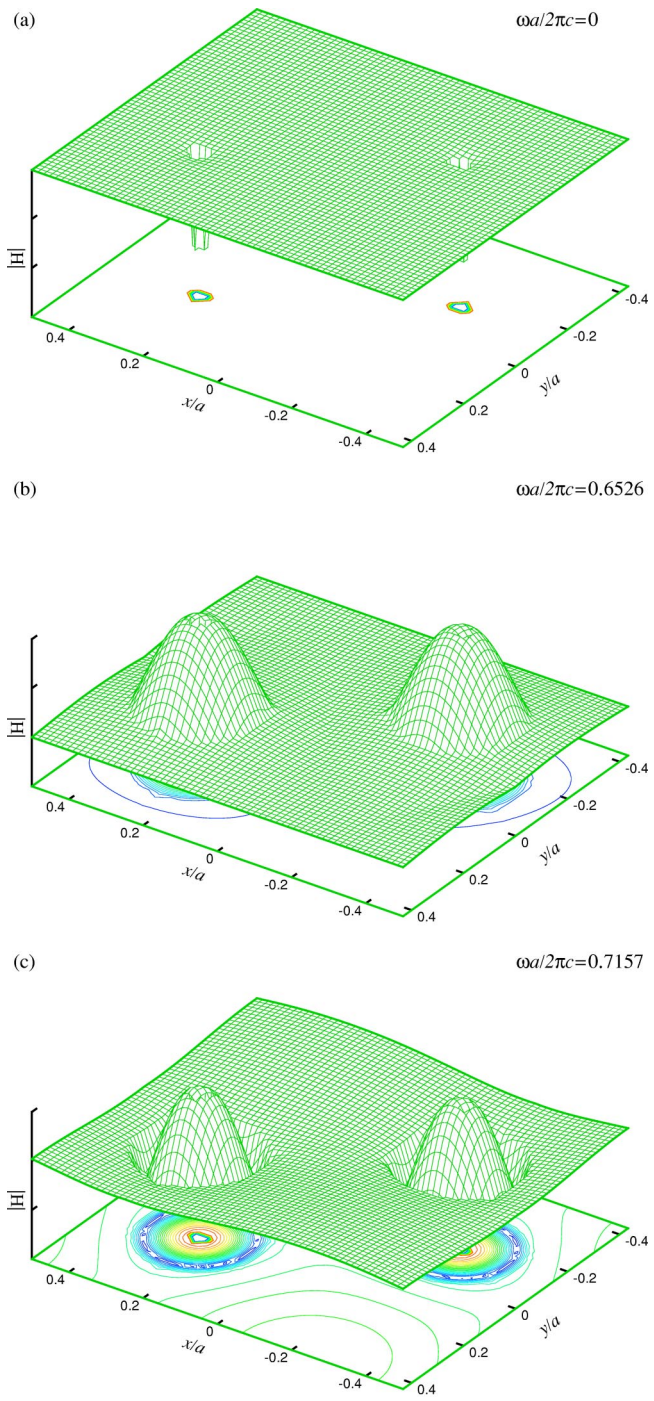

FIG. 13. (Color online) The first three TE eigenfunctions in magnitude at point Γ for the metallodielectric photonic crystal in Fig. 3(a) with $r_i/a=0.02$.

TM modes also exists, as in the case of metallic inclusion in the dielectric region. But the shifted TM bands do not trespass into the original band gap region of the dielectric photonic crystal, and the band structure remains in the "on" state. In fact, only the first TM band in a portion near point Γ is substantially shifted upward, while all the other higher bands are changed only slightly. The fields (TM and TE) in the air region are relatively weaker than in the dielectric region, and therefore the effect of metallic inclusion is smaller. Meanwhile, the TE band gap begins to shrink and finally leads the full band gaps to close. Figure 16 shows the detailed band structure for the metallodielectric photonic crystal at $r_i/a=0.005$. In comparison with Fig. 2, the band structure is almost identical to that for the dielectric crystal without metallic inclusion except the first TM band near point Γ. Figure 17 shows another band structure at the larger $r_i/a=0.1$. In this case, the band edges of the TE band gap

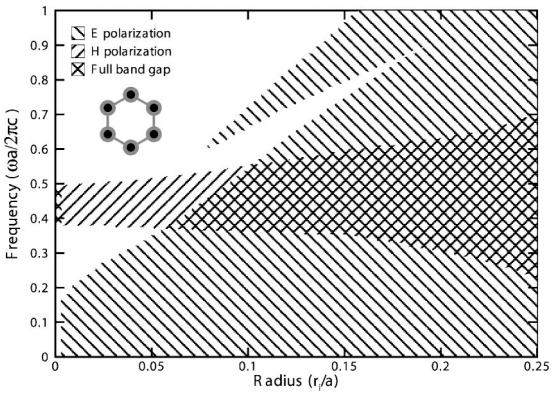

FIG. 14. A map of band gaps computed with a 128×128 grid for the metallodielectric photonic crystal in Fig. 3(a) by varying the radius r_i/a.

become close to each other, making the full band gap smaller.

Next, as an intermediate structure, metallic components are only included in one of two dielectric circular columns for each primitive cell. It is expected that the band structure also behaves in an intermediate manner. This is indeed the case, as shown by the gap map in Fig. 18. The full band gap is not turned off upon inclusion of small metallic components, but is divided into two branches as r_i/a is increased to about 0.014. The upper branch diminishes to zero as r_i/a reaches 0.03, while the lower branch continues to grow gradually in size, which is however smaller than the case of double inclusion (cf. Fig. 14). These behaviors can also be explained as the result of the upward shift of the first two TM bands. As r_i/a is increased from 0, the upward shift is not strong enough to make the first TM band cross the band-gap region of TE modes, while the second TM band does trespass into the region. In trespassing, the second TM band, being narrower in size, does not completely block the band gap of the TE modes, leading to a division of the full band gap into two branches. As r_i/a is further increased, the upward shift of the second TM band eventually makes the upper branch disappear. At large r_i/a, the band structure is the balanced result of both effects of metallic and dielectric components.

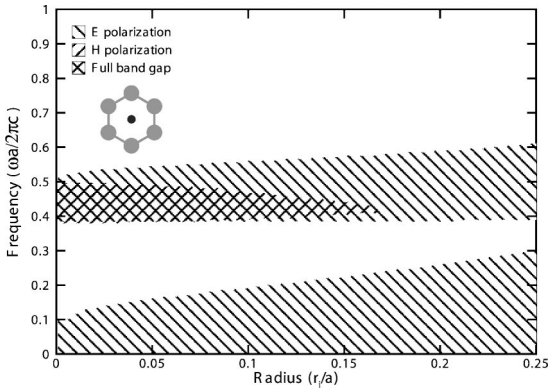

FIG. 15. A map of band gaps computed with a 128×128 grid for the metallodielectric photonic crystal in Fig. 3(b) by varying the radius r_i/a.

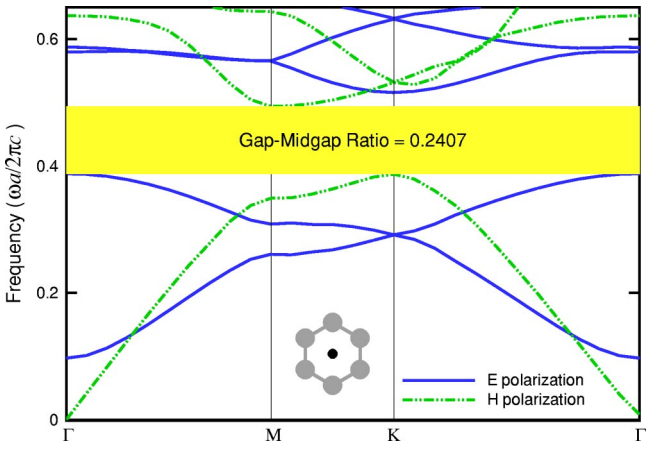

FIG. 16. (Color online) Band structure computed with a 256×256 grid for the metallodielectric photonic crystal in Fig. 3(b) with $r_i/a=0.005$.

Finally, we consider the free-electron model (4) for the metallic components and compute the band structures for E polarization. Figure 19 shows the second eigenfunction in magnitude at point Γ for TM modes for $r_i/a=0.02$ at $\omega_p a/2\pi c=1$. The mode pattern is very similar to Fig. 12(b). It is noticed that the field inside the metal is not forced to zero and the boundary condition (3) is not applied on the metal surface. As a result, the field may somewhat penetrate into the metallic region and no sharp discontinuity exists in the interface. In spite of similarity in mode shapes, the band structures could be very different depending on the plasma frequency. In order to see a trend toward perfect conductors, band structures are presented for $r_i/a=0.01$ at different plasma frequencies $\omega_p a/2\pi c=1$, 4 and 8. At the lower value $\omega_p a/2\pi c=1$, Fig. 20 shows that the band structures are quite different from those presented for the case of perfect conductors in two places: (i) the cutoff frequency of the first band is relatively small, and (ii) the band gap is wide-open between the second and third bands. At the medium value $\omega_p a/2\pi c=4$, Fig. 21 shows that the cutoff frequency becomes larger while the band gap between the second and the third bands

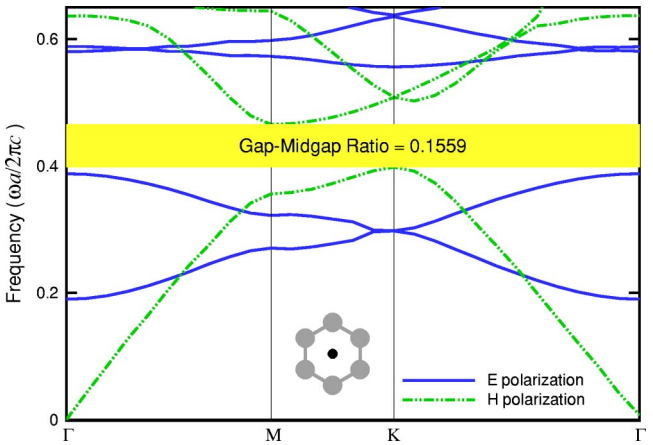

FIG. 17. (Color online) Band structure computed with a 256×256 grid for the metallodielectric photonic crystal in Fig. 3(b) with $r_i/a=0.1$.

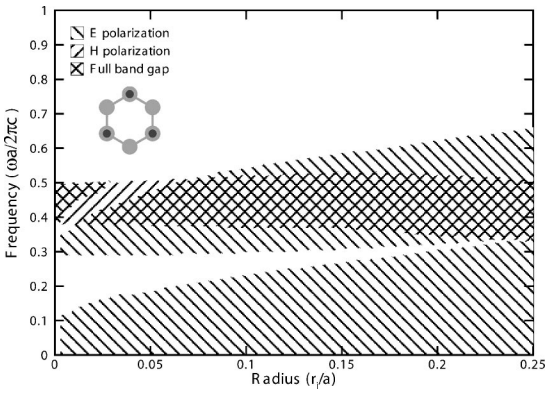

FIG. 18. A map of band gaps computed with a 128×128 grid for the intermediate metallodielectric photonic crystal by varying the radius r_i/a.

becomes smaller. At the large value $\omega_p a/2\pi c=8$, Fig. 22 shows that the cutoff frequency is even larger and has the value 0.188 which is pretty close to 0.211 in Fig. 6 for perfect conductors, while the band gap between the second and the third bands is now very small. A close comparison between Fig. 22 (free-electron model) and Fig. 6 (perfect conductors) shows that the whole band structures for TM modes are in close agreement with each other. These trends are expected because as the plasma frequency becomes larger, the dielectric function becomes more negative. Equivalently, the index of refraction is purely imaginary and large in magnitude. The fields inside the metallic region are therefore evanescent modes. In the limit of perfect conductors, the evanescent field is completely expelled from the metal and vanishes there.

IV. CONCLUDING REMARKS

In this study, we have extended an inverse method with multigrid acceleration[39] to compute the band structures of two-dimensional metallodielectric photonic crystals. The present article is focused on the effect of metallic inclusion in a dielectric photonic crystal. The metallic components are first modeled as perfectly conducting materials. In particular, we consider two cases of inclusion: metals (i) inside dielectric circular columns, or (ii) in the air region of a hexagonal lattice made of silicon and air ($\varepsilon/\varepsilon_0=13$). The two types of inclusion have completely different effects on the band structures and gaps. In the case (i), the full band gap is suddenly "turned off" upon metallic inclusion, remaining in the "off" state until the radius of inclusion reaches a threshold value, making its appearance again with further increasing the radius, and eventually behaving like metallic photonic crystals. For the case (ii), the full band gap only changes slightly in size upon metallic inclusion, but gradually diminishes to zero with increasing the radius of inclusion. These different trends of behavior have been successfully explained on a unified basis by examining the different types of boundary conditions for TM and TE modes at metal surfaces, and employing a variational analysis based on Rayleigh's quotients for the TM and TE modes. Moreover, intermediate dielectric photonic crystals are shown to exhibit intermediate behaviors in the band structures.

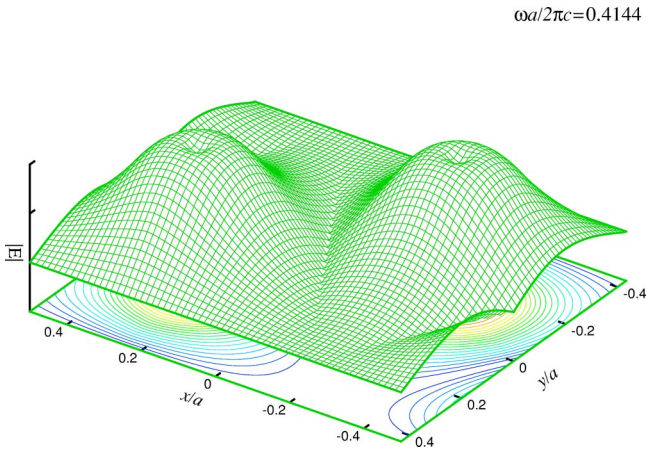

FIG. 19. (Color online) The second eigenfunction in magnitude at point Γ for the metallodielectric photonic crystal (free-electron model) in Fig. 3(a) with $r_i/a=0.02$ and $\omega_p a/2\pi c=1$.

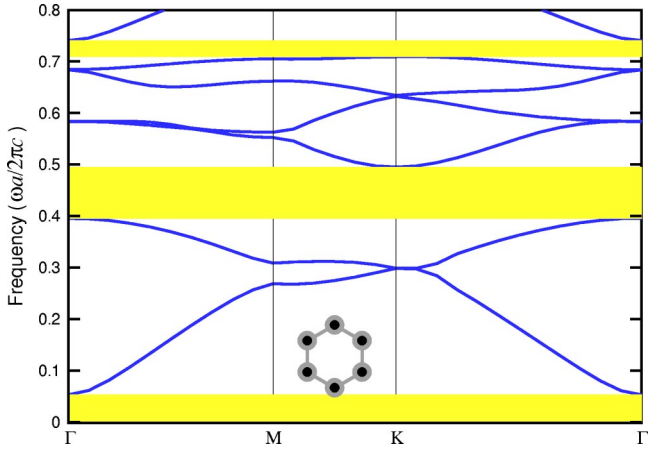

FIG. 20. (Color online) A band structure computed with a 256×256 grid for the metallodielectric photonic crystal (free-electron model) in Fig. 3(a) with $r_i/a=0.01$ and $\omega_p a/2\pi c=1$.

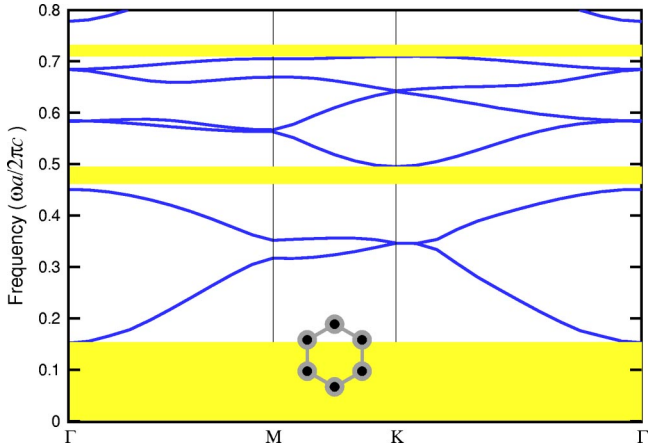

FIG. 21. (Color online) Band structure computed with a 256×256 grid for the metallodielectric photonic crystal (free-electron model) in Fig. 3(a) with $r_i/a=0.01$ and $\omega_p a/2\pi c=4$.

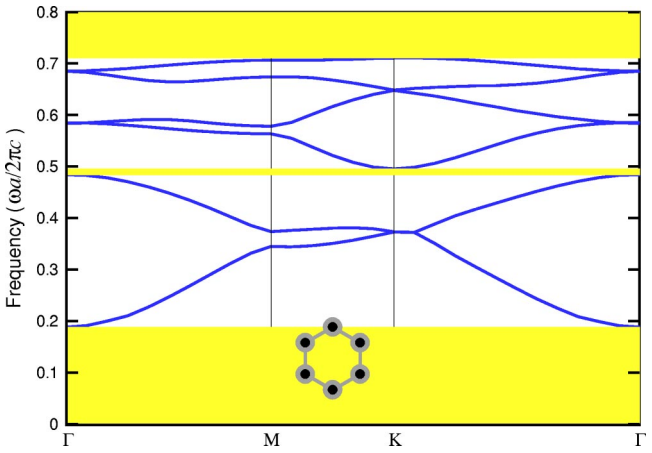

FIG. 22. (Color online) Band structure computed with a 256 $\times$256 grid for the metallodielectric photonic crystal (free-electron model) in Fig. 3(a) with $r_i/a=0.01$ and $\omega_p a/2\pi c=8$.

The perfectly conducting materials as metallic inclusion present an ideal case for studying the metallic shielding effects on photonic structures. More real and complicated phenomena may resort to the study of dispersive, and even dissipative effects of metallic materials. In this study, we also consider the dispersive free-electron model and compute the band structures for the modes of *E* polarization. The numerical results are presented at different plasma frequencies $\omega_p a/2\pi c$. It is shown that as $\omega_p a/2\pi c$ becomes large, these modes show close similarity to those computed for the metallic components modeled as perfect conductors. However, the present method cannot be applied straightforwardly to compute band structures of *H* polarization. On one hand, computation of the band structures of *H* polarization cannot be obviously recast to a standard eigenvalue problem: the eigenfunctions no longer constitute an orthogonal family in the ordinary sense. On the other hand, computation of the modes of *H* polarization is further complicated by the existence of resonant modes near the surface plasmon frequency. This special feature associated only with the *H* polarization has been studied using finite-difference time-domain method[34] and multiple multipole method.[37] The latter reference might suggest that in the present formulation the eigenvalue problem of the *H* polarization could be attacked by the technique of detection used in nonlinear eigenvalue problems. For dissipative metallic materials, both the dielectric function and eigenfrequencies become complex. In addition to the plasma frequency, the relaxation time of the free electron may also play important roles on the dispersion relations of metallic photonic crystals (cf. Refs. 34 and 37). These more challenging topics are currently being under investigation, and the results will be reported elsewhere.

Finally, some comments are available for possible fabrication of the proposed metallodielectric photonic crystals. The following procedures of microelectronics fabrication technology[14,47] may serve this purpose. In the first phase, the silicon is deposited, patterned, and etched to the desired depth for the region of metallic components. In the second phase, the metal is deposited with high pressure, and processed by chemical mechanical polishing.[48] In the third phase, the silicon and metal is patterned and etched for the air region. Then, the surface is processed by chemical mechanical polishing to improve the surface quality.

ACKNOWLEDGMENTS

This work was supported in part by Industrial Technology Research Institute under Contract No. 92S-23-N0, National Science Council of the Republic of China under Contract No. NSC 91-2212-E-002-072, and the Ministry of Economic Affairs of the Republic of China under Contract No. MOEA 92-EC-17-A-08-S1-0006.

[1] E. Yablonovitch, Phys. Rev. Lett. **58**, 2059 (1987).
[2] S. John, Phys. Rev. Lett. **58**, 2486 (1987).
[3] J. D. Joannoupoulos, R. D. Meade, and J. N. Winn, *Photonic Crystals* (Princeton University Press, Princeton, 1995).
[4] K. Sakoda, *Optical Properties of Photonic Crystals* (Springer-Verlag, Berlin, 2001).
[5] S. Lin and G. Arjavalingam, J. Opt. Soc. Am. B **11**, 2124 (1994).
[6] T. F. Krauss, R. M. De La Rue, and S. Brand, Nature (London) **383**, 699 (1996).
[7] J. S. Foresi, P. R. Villeneuve, J. Ferrera, E. R. Thoen, G. Steinmeyer, S. Fan, J. D. Joannopoulos, L. C. Kimerling, H. I. Smith, and E. P. Ippen, Nature (London) **390**, 143 (1997).
[8] A. Mekis, J. C. Chen, I. Kurland, S. Fan, P. R. Villeneuve, and J. D. Joannopoulos, Phys. Rev. Lett. **77**, 3787 (1996).
[9] O. Painter, R. K. Lee, A. Scherer, A. Yariv, J. D. O'Brien, P. D. Dapkus, and I. Kim, Science **284**, 1819 (1999).
[10] J. C. Knight, J. Broeng, T. A. Birks, and P. St. J. Russell, Science **20**, 1476 (1998).
[11] D. L. Bullock, C. Shih, and R. S. Margulies, J. Opt. Soc. Am. B **10**, 399 (1993).
[12] E. R. Brown and O. B. McMahon, Appl. Phys. Lett. **67**, 2138 (1995).
[13] S. Fan, P. R. Villeneuve, and J. D. Joannopoulos, Phys. Rev. B **54**, 11 245 (1996).
[14] J. G. Fleming, S. Y. Lin, I. El-Kady, R. Biswas, and K. M. Ho, Nature (London) **417**, 52 (2002).
[15] X. Zhang, Z. Q. Zhang, L. M. Li, C. Jin, D. Zhang, B. Man, and B. Cheng, Phys. Rev. B **61**, 1892 (2000).
[16] A. R. McGurn and A. A. Maradudin, Phys. Rev. B **48**, 17 576 (1993).
[17] D. R. Smith, S. Schultz, N. Kroll, M. Sigalas, K. M. Ho, and C. M. Soukoulis, Appl. Phys. Lett. **65**, 645 (1997).
[18] D. Sievenpiper, L. Zhang, R. F. J. Broas, N. G. Alexopolous, and E. Yablonovitch, IEEE Trans. Microwave Theory Tech. **47**, 2059 (1999).
[19] J. R. Sirigiri, K. E. Kreischer, J. Machuzak, I. Mastovsky, M. A. Shapiro, and R. J. Temkin, Phys. Rev. Lett. **86**, 5628 (2001).
[20] D. F. Sievenpiper, M. E. Sickmiller, and E. Yablonovitch, Phys.

Rev. Lett. **76**, 2480 (1996).
[21] A. Moroz, Phys. Rev. Lett. **83**, 5274 (1999).
[22] D. F. Sievenpiper, E. Yablonovitch, J. N. Winn, S. Fan, P. R. Villeneuve, and J. D. Joannopoulos, Phys. Rev. Lett. **80**, 2829 (1998).
[23] T. W. Ebbesen, H J. Lezec, H. F. Ghaemi, T. Thio, and P. A. Wolff, Nature (London) **391**, 667 (1998).
[24] J. B. Pendry, A. J. Holden, W. J. Stewart, and I. Youngs, Phys. Rev. Lett. **76**, 4773 (1996).
[25] F. J. Garcia-Vidal and J. B. Pendry, Phys. Rev. Lett. **77**, 1163 (1996).
[26] J. B. Pendry, Phys. Rev. Lett. **85**, 3966 (2000).
[27] A. Moroz, Phys. Rev. B **66**, 115109 (2002).
[28] E. I. Smirnova, C. Chen, M. A. Shapiro, J. R. Sirigiri, and R. J. Temkin, J. Appl. Phys. **91**, 960 (2002).
[29] V. Kuzmiak, A. A. Maradudin, and F. Pincemin, Phys. Rev. B **50**, 16 835 (1994).
[30] T. Suzuki and P. K. L. Yu, Phys. Rev. B **57**, 2229 (1998).
[31] W. C. Sailor, F. M. Mueller, and P. R. Villeneuve, Phys. Rev. B **57**, 8819 (1998).
[32] J. B. Pendry and A. MacKinnon, Phys. Rev. Lett. **69**, 2772 (1992).
[33] K. Sakoda, N. Kawai, T. Ito, A. Chutinan, S. Noda, T. Mitsuyu, and K. Hirao, Phys. Rev. B **64**, 045116 (2001).
[34] T. Ito and K. Sakoda, Phys. Rev. B **64**, 045117 (2001).
[35] M. Qiu and S. He, J. Appl. Phys. **87**, 8268 (2002).
[36] N. A. Nicorovici, R. C. McPhedran, and L. C. Botten, Phys. Rev. E **52**, 1135 (1995).
[37] E. Moreno, D. Erni, and C. Hafner, Phys. Rev. B **65**, 155120 (2002).
[38] J. Arriaga, A. J. Ward, and J. B. Pendry, Phys. Rev. B **59**, 1874 (1999).
[39] R. L. Chern, C. C. Chang, C. C. Chang, and R. R. Hwang, Phys. Rev. E **68**, 026704 (2003).
[40] R. L. Chern, C. C. Chang, C. C. Chang, and R. R. Hwang, Jpn. J. Appl. Phys. **43**, 3484 (2004).
[41] J. D. Jackson, *Classical Electrodynamics*, 3rd ed. (Wiley, New York, 1999).
[42] B. N. Parlett, *The Symmetric Eigenvalue Problem* (SIAM, Philadelphia, 1998).
[43] G. H. Golub and C. F. Van Loan, *Matrix Computations*, 3rd ed. (Johns Hopkins University Press, London, 1996).
[44] J. W. Demmel, *Applied Numerical Linear Algebra* (SIAM, Philadelphia, 1997).
[45] U. Trottenberg, C. Oosterlee, and A. Schüller, *Multigrid* (Academic, London, 2001).
[46] C. A. Balanis, *Advanced Enginerring Electromechanics* (Wiley, New York, 1989).
[47] S. Y. Lin, J. G. Fleming, D. L. Hetherington, B. K. Smith, R. Biswas, K. M. Ho, M. M. Sigalas, W. Zubrzycki, S. R. Kurtz, and J. Bur, Nature (London) **394**, 251 (1998).
[48] W. Patrick, W. Guthrie, C. Standley, and P. Schiable, J. Electrochem. Soc. **138**, 1778 (1991).